

Monolithic-to-focal evolving biointerfaces in tissue regeneration and bioelectronics

Received: 7 April 2023

Accepted: 22 November 2023

Published online: 11 January 2024

 Check for updates

Jiuyun Shi^{1,11}, Yiliang Lin^{1,2,11}, Pengju Li³, Phil Mickel⁴, Changxu Sun³, Kavita Parekh¹, Jingcheng Ma^{1,2}, Saehyun Kim¹, Brennan Ashwood¹, Lingyuan Meng^{1,3}, Yanqi Luo^{1,5}, Si Chen^{1,5}, Hsiu-Ming Tsai⁶, Candace M. Cham^{1,7}, Jing Zhang², Zhe Cheng¹, Jabr A. Abu-Halimah¹, Jiwang Chen⁸, Philip Griffin³, Eugene B. Chang^{1,7}, Petr Král^{1,4,9}✉, Jiping Yue¹✉ & Bozhi Tian^{1,2,10}✉

Material–biology interfaces are elemental in disease diagnosis and treatment. While monolithic biointerfaces are easier to implement, distributed and focal interfaces tend to be more dynamic and less invasive. Here, using naturally occurring precursors, we constructed a granule-releasing hydrogel platform that shows monolithic-to-focal evolving biointerfaces, thus expanding the forms, delivery methods and application domains of traditional monolithic or focal biointerfaces. Individual granules were embedded in a responsive hydrogel matrix and then converted into various macroscopic shapes such as bandages and bioelectronics–gel hybrids to enhance macroscopic manipulation. The granules can be released from the macroscopic shapes and establish focal bio-adhesions *ex vivo* and *in vivo*, for which molecular dynamics simulations reveal the adhesion mechanism. With the evolving design, we demonstrate that granule-releasing hydrogels effectively treat ulcerative colitis, heal skin wounds and reduce myocardial infarctions. Furthermore, we demonstrate improved device manipulation and bio-adhesion when granule-releasing hydrogels are incorporated into flexible cardiac electrophysiology mapping devices. This work presents an approach for building dynamic biointerfaces.

The interfaces between biomaterials and dynamic biological tissues are essential to disease diagnosis and treatment.^{1–7} Current strategies to promote tight biointerfaces rely mainly on thin, flexible membranes with low bending stiffness, such as those developed for flexible bioelectronics^{8,9}, and the addition of biocompatible or biodegradable adhesives^{10,11}. Recent research has shown that viscoelastic polymers or hydrogels

provide conformal biointerfaces with improved signal transmission and biocompatibility^{12,13}. These monolithic or interconnected constructs, such as mesh devices or hydrogel membranes, can easily reside on an organ-level target in conformity with the target's surface curvature.

However, a mobile, transient and micrometre-scale biomaterial capable of interacting with surrounding cells or tissues would offer

¹Department of Chemistry, University of Chicago, Chicago, IL, USA. ²The James Franck Institute, University of Chicago, Chicago, IL, USA. ³Pritzker School of Molecular Engineering, University of Chicago, Chicago, IL, USA. ⁴Department of Chemistry, University of Illinois at Chicago, Chicago, IL, USA. ⁵Advanced Photon Source, Argonne National Laboratory, Lemont, IL, USA. ⁶Department of Radiology, University of Chicago, Chicago, IL, USA. ⁷Department of Medicine, University of Chicago, Chicago, IL, USA. ⁸Cardiovascular Research Center, University of Illinois at Chicago, Chicago, IL, USA. ⁹Departments of Physics, Pharmaceutical Sciences, and Chemical Engineering, University of Illinois at Chicago, Chicago, IL, USA. ¹⁰The Institute for Biophysical Dynamics, University of Chicago, Chicago, IL, USA. ¹¹These authors contributed equally: Jiuyun Shi, Yiliang Lin. ✉e-mail: pkral@uic.edu; jipingyue@uchicago.edu; btian@uchicago.edu

a more dynamic and less invasive biointerface¹⁴. Focal, cellular-scale biointerfaces would also, by design, provide the interstitial space required for cellular proliferation and migration and physiological signal transmission, unlike monolithic interfaces, which often require degradation before infiltration by cells or biomolecules¹⁵. Such focal biointerfaces would thus enhance tissue regeneration¹⁶ and the efficiency of biomedical devices.

There are both challenges and opportunities associated with the design of materials for transient, cellular-scale biointerfaces in physiological environments. First, the biomaterials are typically prepared with microscopic cell-size-matched features for *in vivo* delivery, which limits their forms (for example, unlikely to be a macroscopic patch) and handling methods^{17,18}. Second, the highly dynamic and heterogeneous cellular microenvironment undergoes constant remodeling¹⁹, including changes to pH, enzymes and other biochemical species. Therefore, it is crucial to ensure that the biointerfacial material shows cellular affinity with dynamic behavior. Third, naturally occurring biopolymers have been explored extensively in the food, pharmaceutical and cosmetic industries due to their biocompatible and biodegradable properties²⁰. These materials may also be used for other applications, including bioelectronics and robotics. It is expected that future cellular-scale biointerfacial materials will demonstrate easier macroscopic handling capability, facilitate cellular-scale adhesion with spatiotemporal control and include a greater amount of naturally occurring elements.

This study demonstrates that a dynamic hydrogel composite can release cellular-size granules in the physiological environments for regenerative medicine and bioelectronics, which has been long sought in the development of hydrogel-based artificial cells²¹. A monolithic-to-focal evolving process allows the composite to harness the properties and functions of both monolithic and focal biointerfaces (Fig. 1a). The hydrogel composites use gelatin and chitosan as the hydrogel matrix to respond to biological environments while also facilitating macroscopic material shaping and manipulation. In addition, the hydrogel composite consists of cellular-scale releasable granules (that is, granular hydrogel) that can form focal bio-adhesions *in vivo* and *ex vivo* and degrade at the end for therapeutic benefit (Fig. 1a and Supplementary Table 1).

The release–adhesion–degradation dynamics of the granule-releasing hydrogels (Fig. 1a) is achieved through (1) modulation of viscoelasticity or enzymatic digestion of the gelatin and chitosan matrix for granular release, (2) drug-inspired surface modification of starch/chitosan-based granules (Fig. 1b) for establishing focal adhesion, and (3) the utilization of naturally occurring and biodegradable biopolymers and biomolecules. Besides the traditional gel forms for injection or coating, granule-releasing hydrogels can also yield bandage-like configurations (Fig. 1c), bioelectronics–hydrogel composites, and hydrogel or aerogel microneedle constructs (Supplementary Fig. 1). The initial macroscale forms of the composites protect fragile electronic components and facilitate flexible bioelectronic device deployment (Fig. 1d,e). Besides, the monolithic matrix permits a tunable viscoelastic environment for slow and responsive granular release. Upon dispersion, the microscale granules with surface modifications would instantiate dispersed biointerfaces. Contrary to monolithic biointerfaces, these dispersed interfaces could potentially facilitate enhanced transport of small molecules such as water, electrolytes and amino acids (Fig. 1a and Supplementary Fig. 2). In addition, the subsequent biodegradation of the natural biopolymer will also promote regenerative tissue recovery (Supplementary Fig. 3). With this evolving mechanism, the granule-releasing hydrogel can effectively manage symptoms of dextran sulfate sodium (DSS)-induced colitis, accelerate skin wound healing, and facilitate cardiac tissue regeneration and mapping of cardiac activity with bioelectronic devices (Fig. 1a,f). This evolving system integrates the benefits and application domains of the current monolithic and focal biointerfacing materials and devices.

Results

Tunable viscoelasticity enables responsive granule release

To build the granule-releasing hydrogels, we used naturally derived starch, chitosan and gelatin (Supplementary Table 1). The gelatin forms a three-dimensional hydrogel network that confines the starch/chitosan granules for initial macroscopic manipulation. Upon release, the cellular-scale granules (Fig. 1a and Supplementary Fig. 4) would penetrate into deep and narrow tissue regions (for example, wound site, intestinal lumen) not easily accessed by traditional bulky hydrogels²². We first characterized the morphology and dynamics of the granule-releasing hydrogels. It has been reported that chitosan interacts with starch granules through intermolecular interactions²³. Using metal labeling and synchrotron-based three-dimensional X-ray fluorescence tomography, we examined the structure of individual starch/chitosan granules and revealed the patchy distribution of chitosan on the surface of the starch-based granules (Fig. 2a and Supplementary Fig. 2). The surface-attached chitosan provides an easier chemical anchor point for further modification as the amine groups of the chitosan are more reactive than the hydroxyl groups of the starch²⁴. When embedded inside the hydrogel matrix, the granules are evenly distributed, as revealed by confocal microscopy and scanning electron microscopy (Fig. 2b and Supplementary Fig. 5).

The initial biointerface construction would benefit from a conformal biomaterial with tissue-like mechanical behavior²⁵. The as-prepared granule-releasing hydrogel has a high water content (>70%), suitable softness (Young's modulus of 80 kPa, similar to wound tissue and cardiac muscles²⁶) and moderate stretchability (maximum strain >100%; Supplementary Fig. 6). The granule-releasing hydrogels also show tissue-like viscoelastic behavior as evidenced by strain- and frequency-dependent moduli, fast stress relaxation and large mechanical hysteresis (Fig. 2c and Supplementary Figs. 7 and 8), which largely assists in forming conformal interfaces with curvilinear surfaces¹². The observed viscoelastic behavior can be primarily attributed to the rearrangement of the granules under the external stress and the microstructural reorganization of granules within the matrix which provides enhanced energy dissipation²⁷.

To establish the evolving biointerfaces, the granule-releasing hydrogels should release the granules at the targeted biointerface in response to diverse stimuli. We first investigate how temperature variations shift the viscoelastic properties and facilitate granular release (Fig. 2d and Supplementary Fig. 9). We examined rheological changes across a temperature ramp to understand the rheological response to temperature (Fig. 2e–g and Supplementary Figs. 10 and 11). The contour map (Fig. 2g) illustrates that the granule-releasing hydrogel can transform and reconstruct itself under physiological conditions. This is largely due to the gelation behavior of gelatin-based polymers²⁸, which enables a sharp decrease in the storage modulus as the temperature changes from 25 °C to 40 °C, and release of the encapsulated starch granules. We also performed *in situ* Fourier-transform infrared (FTIR) spectroscopy on the granule-releasing hydrogel, applying heavy water to reveal hydrogen-bond associations during the phase transition of the gelatin polymer (Fig. 2g and Supplementary Table 2). During heating from 1 °C to 65 °C, we observed the disappearance of spectral features in the amide I region from 1,600 cm⁻¹ to 1,700 cm⁻¹ (Supplementary Fig. 12). These results suggest that the loss of intermolecular hydrogen bonds between gelatin polymer chains allows the dynamic transition of the hydrogel and granule release at body temperature. Singular value decomposition analysis further confirmed that the gelation points were at ~30.9 °C during temperature ramp-up. (Supplementary Fig. 13). The granule-releasing hydrogel also shows responsiveness to pH at different temperatures (Fig. 2e–h and Supplementary Fig. 14). We attribute the pH responsiveness of the granule-releasing hydrogel to the protonation–deprotonation balance between amino groups in gelatin and chitosan²⁹. We found that the pH variations can largely change the granular transport behavior, which modulates the releasing behavior of the granular composite in different pH environments (Fig. 2h).

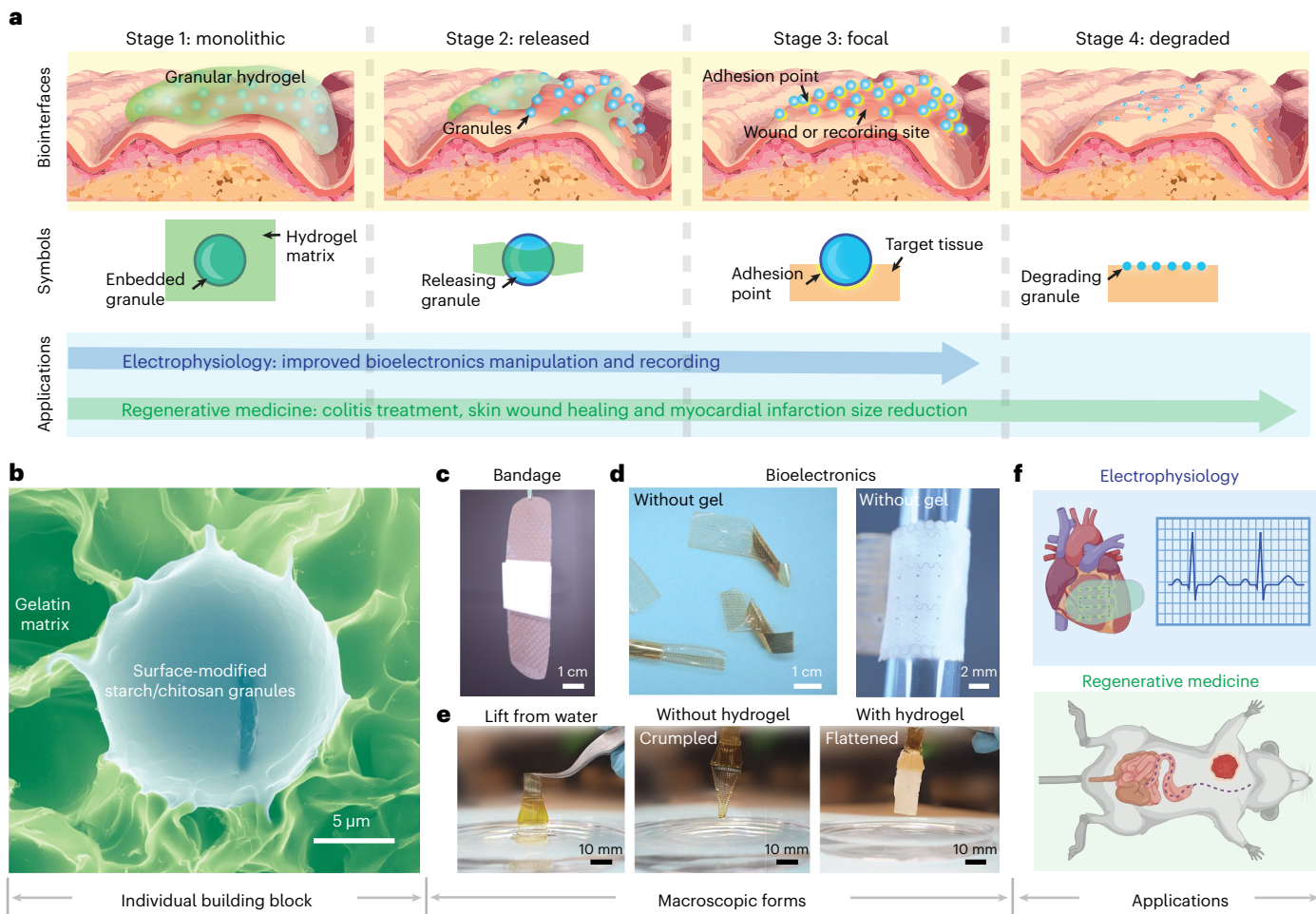


Fig. 1 | The dynamic hydrogel system forms a granular biointerface for diagnosis and therapy. **a**, Schematic of the dynamic processes involved in the construction of the granular distributed biointerface. Stage 1: the viscoelastic granule-releasing hydrogel conforms to the underlying tissue. Stage 2: the granule-releasing hydrogel releases the granular composites to the tissue surface based on the physiological environment cues. Stage 3: the released granular composites anchor or dock on the tissue surface through the biological affinitive surface. Stage 4: the degradation fragments of granules are beneficial for tissue repair and regeneration. **b**, Scanning electron microscopy

image of an individual granule (blue) inside the hydrogel matrix (green). **c,d**, The granule-releasing hydrogels could take on various forms for diverse applications. **c**, Integrated with a medical bandage. **d**, Hybridized with fragile bioelectronic devices (left) for a mechanically robust cardiac recording device (right). **e**, The granule-releasing hydrogel enhances the manipulation of thin-film bioelectronics. **f**, The granule-releasing hydrogel systems perform different biological tasks, including mitigation of inflammatory bowel disease, skin wound healing, cardiac signal recording and cardiac tissue regeneration.

Drug-inspired surface modifications for focal bio-adhesion

The evolving granule-releasing hydrogels allow the motion and release of granules in the physiological environment. To enhance adhesion at granule-based focal biointerfaces, we further chemically modified the granular composites with a variety of naturally occurring drug molecules, including aspirin, niacin and butyrate (Supplementary Table 1). These molecules have rapid and high oral absorption ability and efficiently interact with the phospholipid membrane and extracellular matrix, two major components of the tissues. Inspired by this, we hypothesized that surface modification of the granules with these drug molecules would enhance biointerface adhesion, regardless of the therapeutic effects of the molecules themselves.

Using molecular dynamics simulations, we found that drug molecules with rapid absorption and lipophilicity³⁰, such as aspirin, can promote binding between chitosan and the lipid bilayer by reducing the interaction energy (Fig. 3a). Specifically, the time averaged per-chain interaction energy between one aspirin-modified chitosan chain and 1,2-dimyristoyl-sn-glycero-3-phosphocholine (DMPC) membrane is $\Delta E = -5.67 \pm 2.20 \text{ kcal mol}^{-1}$, while the average

interaction energy between unmodified chitosan and DMPC membrane is $-3.52 \pm 1.79 \text{ kcal mol}^{-1}$.

We synthesized the aspirin–chitosan bioconjugate using carbodiimide chemistry (Fig. 3b) and formed the aspirin-modified chitosan/starch granules (AS). NMR and FTIR spectroscopy measurements confirmed successful synthesis (Supplementary Figs. 15 and 16). To investigate the intrinsic affinities between different granules and diverse biological components (Fig. 3c), we employed aqueous granular suspensions without involving gelatin hydrogel matrix and found that the AS showed the strongest affinity. First, we performed the flow adhesion tests in vitro where the fluid flow shear stress mimics the luminal shear stress of the body³¹. Specifically, AS showed a higher retention rate than the unmodified starch/chitosan granules (SC) and pure starch granules (starch) when flowing over different biological components (Fig. 3c), including molecular assemblies (phospholipid layer, Fig. 3c(i); collagen layer, Fig. 3c(ii)), in vitro cell monolayers (human colorectal adenocarcinoma cell line Caco2, Fig. 3c(iii); human immortalized keratinocytes cell line HaCaT, Fig. 3c(iv)), and in vitro intestinal organoids (mouse colon organoid, Fig. 3c(v); human ileum organoid, Fig. 3c(vi)).

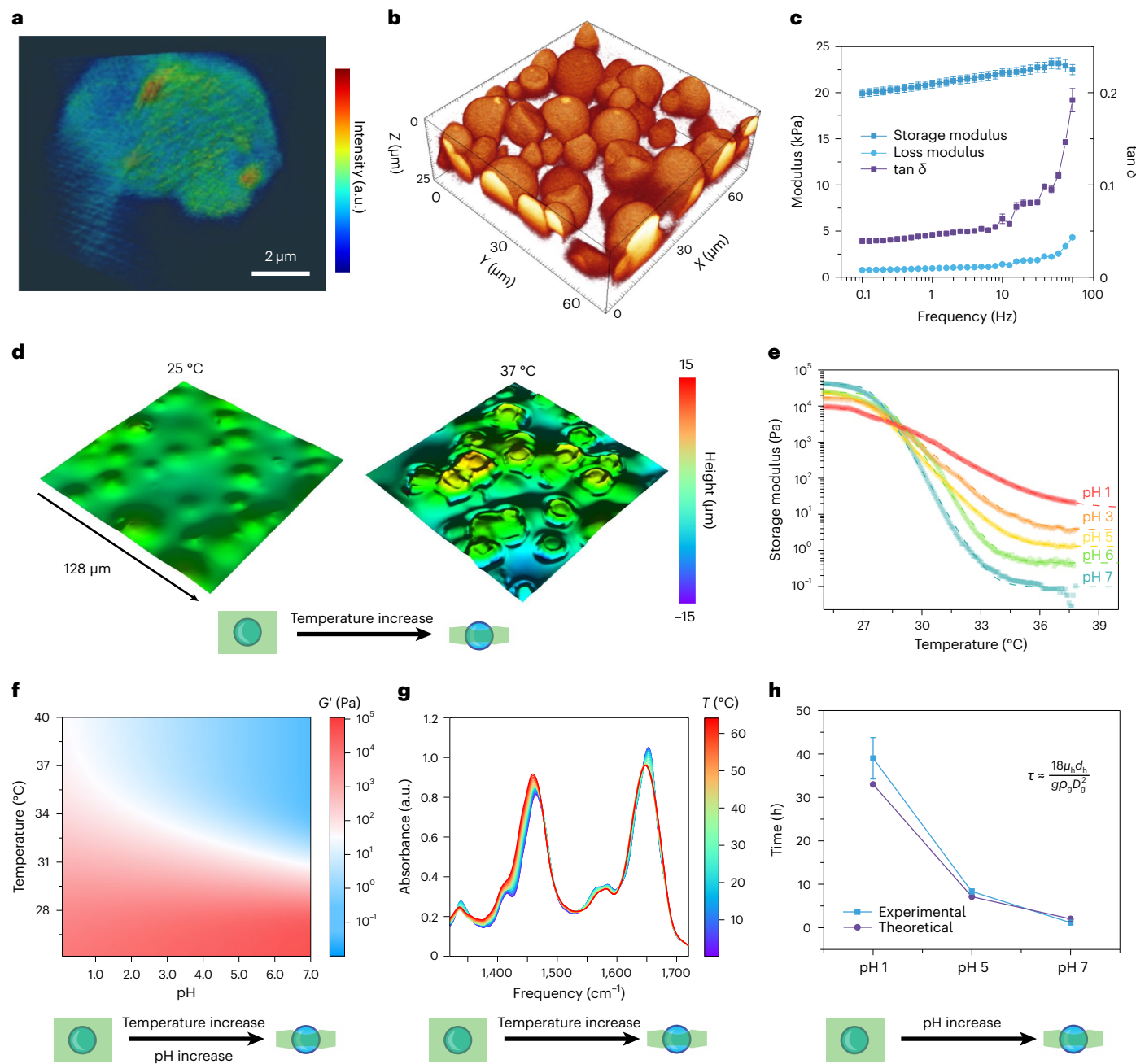


Fig. 2 | The granule-releasing hydrogel shows dynamic mechanical behavior and responsiveness for granular transport. **a**, Three-dimensional ptychographic tomography showing the molecular distribution of chitosan on the surface of starch granules. The color bar indicates the intensity of the chitosan signal. **b**, Confocal image of a granule-releasing hydrogel showing that the starch granules are physically proximate to the polymeric matrix, indicating potential interactions between the granules and supportive matrices. **c**, Rheological analysis shows that the granule-releasing hydrogels are soft and viscoelastic. Storage modulus (G' ; left axis), loss modulus (G'' ; left axis) and $\tan \delta$ (G'/G'' ; right axis) are shown as a function of frequency at 1% strain. $n = 3$ independent experiments. **d**, Three-dimensional laser microscopy image showing that the granules are released following the dynamic transition of the granule-releasing hydrogel at body temperature. The color bar indicates height information. **e**, A temperature ramp rheological test shows that the granule-releasing hydrogels respond to both temperature and pH. **f**, Contour map of the hydrogel storage modulus (G') as a function of temperature and pH. The color bar indicates the modulus of the hydrogel. The red regions represent high modulus and the blue regions represent low modulus. **g**, In situ FTIR spectral change confirms the phase transition of gelatin-based hydrogel during heating. The changes in the amide I and II regions (Amide I region: $1520\text{--}1730\text{ cm}^{-1}$; Amide II region: $1320\text{--}1520\text{ cm}^{-1}$) indicate a loss of triple helix structure and formation of intermolecular hydrogen bonding between gelatin and heavy water. The color bar indicates the measurement temperature. **h**, Experimental and theoretical analysis indicates that the granular transport process at body temperature is influenced by the environmental pH. $n = 3$ independent experiments. All data are presented as mean values \pm s.d.

the height information. **e**, A temperature ramp rheological test shows that the granule-releasing hydrogels respond to both temperature and pH. **f**, Contour map of the hydrogel storage modulus (G') as a function of temperature and pH. The color bar indicates the modulus of the hydrogel. The red regions represent high modulus and the blue regions represent low modulus. **g**, In situ FTIR spectral change confirms the phase transition of gelatin-based hydrogel during heating. The changes in the amide I and II regions (Amide I region: $1520\text{--}1730\text{ cm}^{-1}$; Amide II region: $1320\text{--}1520\text{ cm}^{-1}$) indicate a loss of triple helix structure and formation of intermolecular hydrogen bonding between gelatin and heavy water. The color bar indicates the measurement temperature. **h**, Experimental and theoretical analysis indicates that the granular transport process at body temperature is influenced by the environmental pH. $n = 3$ independent experiments. All data are presented as mean values \pm s.d.

Next, in ex vivo experiments, the AS had a higher retention rate than SC when flowing over DSS-treated ulcerative colonic epithelium (Fig. 3c(vii)) or skin wound bed (without epidermis, dermis exposed; Fig. 3c(viii)). Notably, we also found that the size and shape of the granular composite does not significantly influence the retention

rate on the substrate (Supplementary Figs. 17–19). The retention period of the AS was also prolonged in mouse intestinal tracts *in vivo*, indicating potential therapeutic applications (Supplementary Figs. 20 and 21). We also performed a macroscopic lap-shear adhesion test to prove that the aspirin modification increases the adhesion

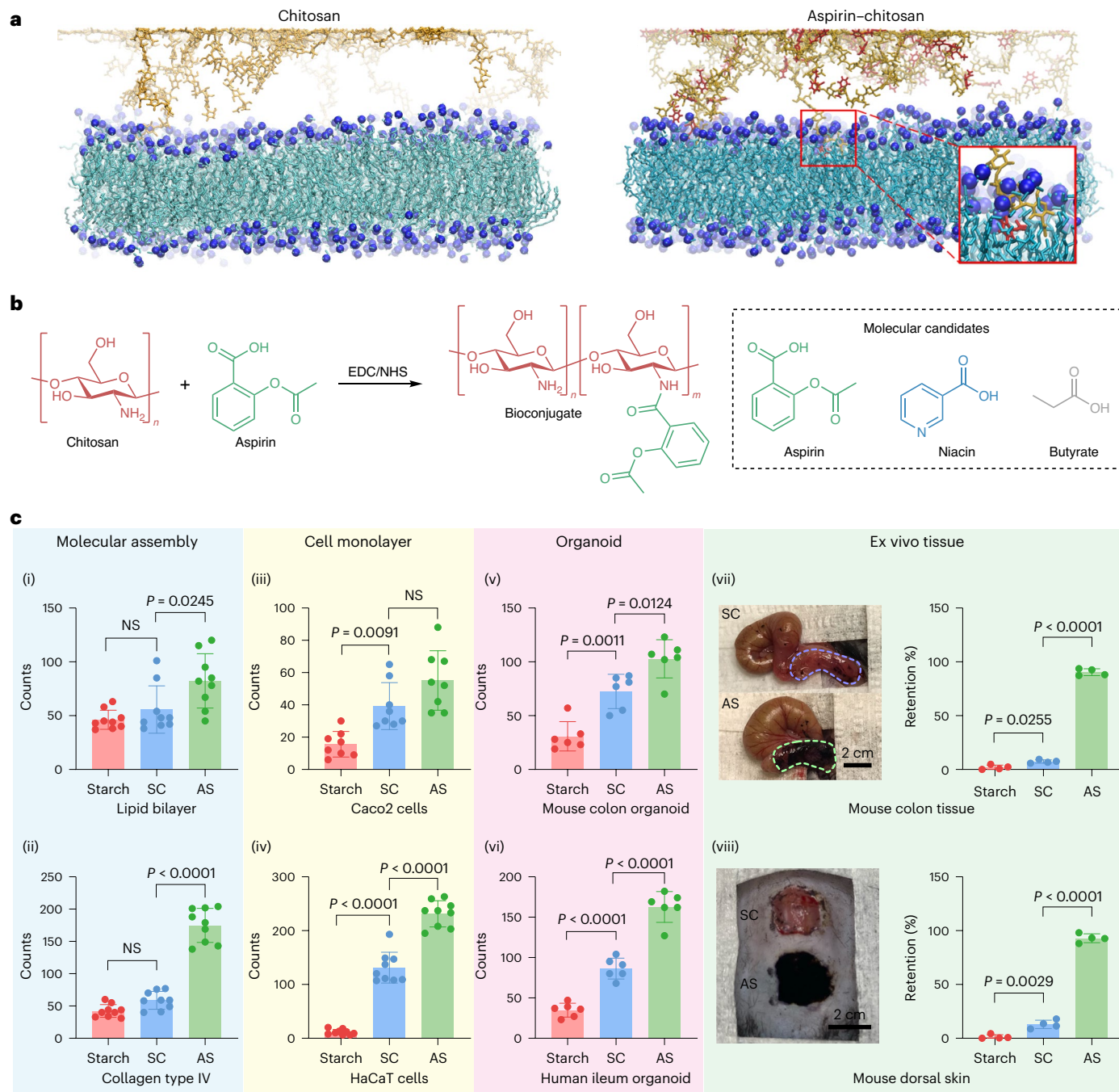


Fig. 3 | Chemical modification of granule composites with bioactive molecules enhances biological affinity. **a**, Atomistic molecular dynamics simulations showing the interaction between unmodified chitosan (left) and aspirin–chitosan bioconjugates (right) with DMPC lipid molecules. Inset: the aspirin-modified chitosan occasionally extends into the lipid membrane. Yellow, chitosan; red, aspirin; blue, hydrophilic head of the lipid molecules; green, hydrophobic tail of the lipid molecules. **b**, Molecular structure of chitosan (red) and aspirin (green) and the route of synthesis for the aspirin–chitosan bioconjugate using N-hydroxysuccinimide (NHS)/1-ethyl-3-(3-

dimethylaminopropyl)carbodiimide (EDC) chemistry. **c**, Flow adhesion tests show that the aspirin-modified starch/chitosan granules (i–viii) enhance starch retention at molecule, cell, organoid and ex vivo tissue levels. Starch, starch granules only; SC, starch/chitosan granules without chemical modification; AS, starch/chitosan granules with aspirin modification. Data are presented as mean \pm s.e.m. In (i), (ii) and (iv), $n = 9$; in (iii), $n = 8$; in (v) and (vi), $n = 6$; in (vii) and (viii), $n = 8$ independent experiments. Pvalues are determined by ordinary one-way ANOVA with Tukey's multiple comparisons test. NS, not significant.

strength of chitosan (Supplementary Fig. 22). Starch/chitosan granules modified with niacin and butyric acid, drug molecules with good oral absorption, also showed affinity for the colon epithelium and skin wound beds (Supplementary Figs. 23 and 24), although with lower efficiency than AS. These results demonstrate that chemical conjugation of biomolecules can enhance adhesion/affinity at granule-based focal biointerfaces and that good oral absorption may be generally

considered a ‘qualitative’ pre-evaluation factor for potential molecular modifications.

Therapeutic effect in an ulcerative colitis model

We sought to determine whether the biophysical barrier formed by the adhered biomolecule-conjugated granules and their partial degradation products at the damaged tissue surface facilitate disease recovery

(Fig. 4a and Supplementary Table 1). Colitis is an inflammatory chronic condition of the colon of unknown cause³². Current treatment options for ulcerative colitis are limited to managing symptoms, which, however, does not address the underlying causes, including the impaired intestinal barrier and dysbiosis of gut microbiota³³. To evaluate the therapeutic effects of the granule-releasing hydrogels (Fig. 4b), we performed a series of pre-clinical evaluations with a DSS-induced colitis model. The DSS-induced colitis model is widely utilized for *in vivo* evaluation given that its clinical and histological features are similar to those of human ulcerative colitis, including adverse symptoms (for example, bleeding, diarrhea), loss of epithelium barrier functions, intestinal inflammation and dysregulated host-gut microbiota³⁴. Using this animal model, we observed that the granules released from an orally administrated aspirin-modified granule-releasing hydrogels (AGH) adhered to DSS-treated colonic epithelium (Fig. 4c). This is consistent with the *ex vivo* mucosal affinity of the AS observed with flow adhesion tests (Fig. 3c). Our results indicate that the granule-releasing hydrogel composites have promising potential in managing DSS-induced ulcerative colitis through the colonic biointerface.

The AGH showed improved therapeutic effects, compared with non-modified yet still dynamic/releasable granule-releasing hydrogels (DGH), in the management of rodent colitis adverse symptoms, in terms of body weight loss, colon length, fecal water content and bleeding scores (Fig. 4d and Supplementary Fig. 25). The non-releasing polyvinyl alcohol matrix hydrogel (PVA) or non-granule-releasing hydrogel (NGH; containing the same chemical compositions) did not show similar levels of therapeutic effects (Supplementary Fig. 26). The granules alone showed positive effects on mouse body weight loss and colon shortening, but not on fecal water content or bleeding scores (Supplementary Fig. 26). Besides, only AGH treatment significantly improved histological colonic damage, but not AS, PVA or NGH (Fig. 4e,f and Supplementary Table 3), indicating the AGH may form a therapeutic biointerface to protect the colonic epithelium against pathological damage. Thus, the granular-releasing process and formation of distributed focal biointerfaces probably have an important role in treating ulcerative colitis.

The AGH form a therapeutic biointerface in the colonic region and help rebuild the colon barrier in mice. We used the fluorescein isothiocyanate (FITC)-dextran permeability assay to explore colon permeability. Four hours after administration of FITC-dextran, the AGH group had less FITC-dextran signal in the blood (Fig. 4g). The reduction in paracellular uptake of large-size molecules from the gastrointestinal tract suggests restoration of intestinal intactness. Histological periodic acid-Schiff (PAS) staining revealed that the thickness of the intestinal epithelium and the goblet cells increased significantly with AGH treatment, suggesting restoration of the mucin layer and intestinal functions (Supplementary Figs. 27 and 28). The chitosan coating may lead to slower granular composite digestion in the stomach and intestine, which prolongs the therapeutic biointerface period in the harsh *in vivo*

environment and protects the ulceration from further damage^{35,36}. It is important to note that, although the AS also shows therapeutic effects in treating ulcerative colitis, these effects are less significant compared with the AGH (Supplementary Figs. 29–31). We primarily attribute the superior therapeutic effect of the AGH group over the AS group to the sustained and pH-responsive release of therapeutic granules within the gastrointestinal tract.

The AGH modulate the composition of gut microbiota. Increasing evidence has shown that dysbiosis of the gut microbiota is closely associated with human gastrointestinal disease and has a key role in the pathogenesis of ulcerative colitis³⁷. Restoration of the healthy gut microbiota could largely regulate the gut immune response and effectively promote recovery from ulcerative colitis³⁸. 16S ribosomal RNA gene sequencing of feces samples demonstrated that both DGH and AGH modulated microbiota diversity, which is supported by the linear discriminant analysis effect size (Fig. 4h and Supplementary Figs. 32 and 33). A principal coordinates analysis plot of beta diversity further revealed that the gut microbiota profiles of AGH group were distinct from the profiles of other groups (Supplementary Fig. 34). At the phylum/family level, the AGH significantly enhanced the relative abundance of *Akkermansia*, *Bifidobacterium* and *Lactobacillus*, all important microbial indicators that are prominently decreased in patients with inflammatory bowel diseases³⁹ (Fig. 4i–l). Specifically, *Akkermansia* contributes to the thickness of the mucin layer, indicating a protective role in intestinal barrier intactness and function⁴⁰. The beneficial role of *Bifidobacterium* and *Lactobacillus*, as probiotics, in ulcerative colitis in both animal models and patients has been widely reported^{41,42}. In addition, we found that the abundance of other gut microbes, such as *Bacteroides* and *Romboutsia*, were also significantly modulated; these findings require further systematic investigation given the limited studies in the literature (Supplementary Fig. 35). We also demonstrated that granule-releasing hydrogels carrying niacin or butyrate modifications formed biointerfaces with colonic tissue and alleviated adverse colitis symptoms in treated DSS-induced colitis (Supplementary Figs. 36–39). Aspirin is known to cause mucosal ulceration and other potential issues in the gut, especially when there is inflammation. However, in our design, aspirin is not in its free molecular form. Its therapeutic effects and toxicity are largely limited when it is conjugated with the proposed granular system⁴³. We report that free aspirin at the same dose as on the conjugated granules, or even at five times the dose, did not have any significant effect on DSS-induced colitis symptoms (Supplementary Fig. 40). Compared with the clinically used drug against conventional inflammatory bowel disease (IBD), 5-aminosalicylic acid, AGH appears to show an improved therapeutic effect (Supplementary Fig. 41). The traditional adhesion method based on catechol also shows the trend in alleviating the adverse colitis symptom (Supplementary Fig. 42). However, the curing conditions for catechol-based adhesives often require oxidants and elevated pH, which might undermine the biocompatibility of the materials in some biomedical applications⁴⁴. Thus,

Fig. 4 | AGH system treats DSS-induced ulcerative colitis *in vivo*. **a**, Schematic of released granules forming temporary biophysical barriers and modulating gut microbiota. **b**, Mice were given 3% DSS in drinking water to induce ulcerative colitis. Granule-releasing hydrogel therapies were orally administrated (10 mg per kg daily). **c**, Microscopy images showing that the Alexa Fluor 488-labelled AGH passed through the gastrointestinal tract and formed a distributed biointerface in the colon. **d**, Mouse body weight over 7 days. AGH-treated mice showed the highest body weights. **e**, Representative images of H&E staining show that pathological damage is significantly diminished in the colons of AGH-treated mice, in terms of epithelium thickness, crypt intactness and inflammation. **f**, Histological score analysis shows that AGH-treated mice have a lower level of histological inflammation and tissue damage. **g**, Left: schematics illustrating that the granular interfaces restore the intestinal permeability. Right: blood levels of FITC-dextran were lowest in AGH-treated mice. **h**, Linear discriminant analysis effect size taxa analysis indicates that the AGH and DGH change the bacterial diversity of DSS-induced colitis mice. Significant (red and green) and non-

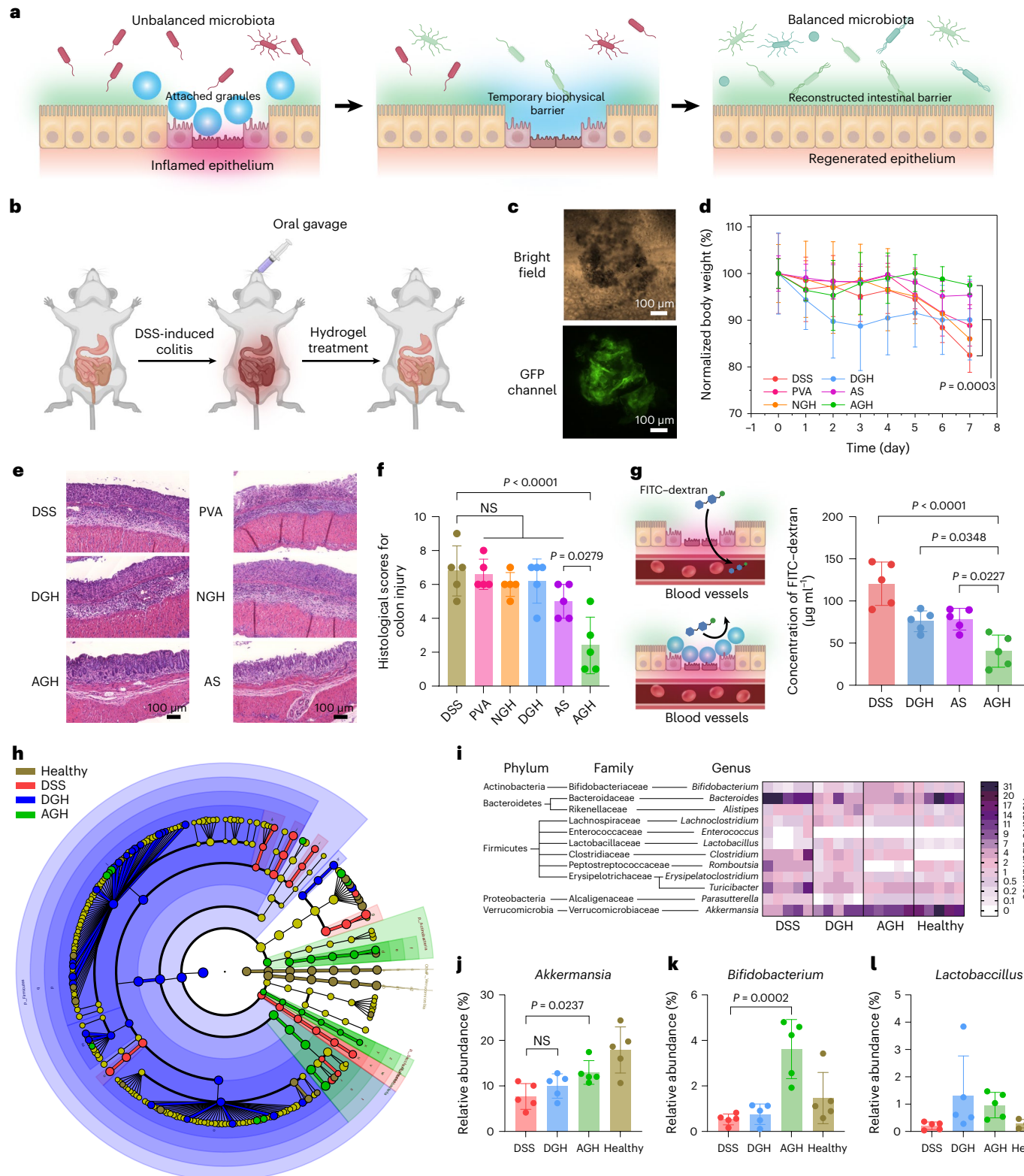
significant (yellow) discriminant taxonomic nodes are colored. Circle diameter is proportional to the taxon's abundance. **i**, Taxonomy relative abundance heatmap shows genus-level taxa (rows) for each mouse (columns). **j–l**, Relative abundance increases are observed for *Akkermansia* (**j**), *Bifidobacterium* (**k**) and *Lactobacillus* (**l**). Control, healthy mice; DSS, mice with DSS-induced colitis, no treatment; PVA, mice with DSS-induced colitis, treated with aspirin-modified starch and chitosan inside polyvinyl alcohol matrix; NGH, mice with DSS-induced colitis, treated with non-granule-releasing hydrogels. The composition of NGH is the same as the AGH, but the granular structure is destroyed through gelatinization process. AS, mice with DSS-induced colitis, treated with aspirin-modified starch and chitosan granules; DGH, mice with DSS-induced colitis, treated with unmodified dynamic granule-releasing hydrogels. AGH, mice with DSS-induced colitis, treated with aspirin-modified granule-releasing hydrogels. Data are presented as mean \pm s.e.m. $n = 5$ independent animals. *P* values are determined by ordinary one-way ANOVA with Tukey's multiple comparisons test.

aspirin modification in our system, allowing for a more dynamic and less invasive interaction with cellular environments, leads to a more effective therapeutic effect. Furthermore, it is worth noting that the gelatin hydrogel alone does not show a therapeutic impact in the treatment of ulcerative colitis (Supplementary Fig. 43). This observation implies that its primary role is facilitative, specifically assisting in the encapsulation and transport of granules. Further fluorescence imaging also confirms that the hydrogel matrix slows down the retention dynamics of granular

composites in the gastrointestinal tract (Supplementary Fig. 44). In summary, the evolving hydrogel system encapsulating chemically modified starch/chitosan granules indicated potential therapeutic effects on the management of acute rodent colitis symptoms.

Therapeutic effect in a skin wound model

Evolving biointerfaces for therapeutic intervention can also be achieved on damaged skin epithelium (Supplementary Table 1). Skin wound



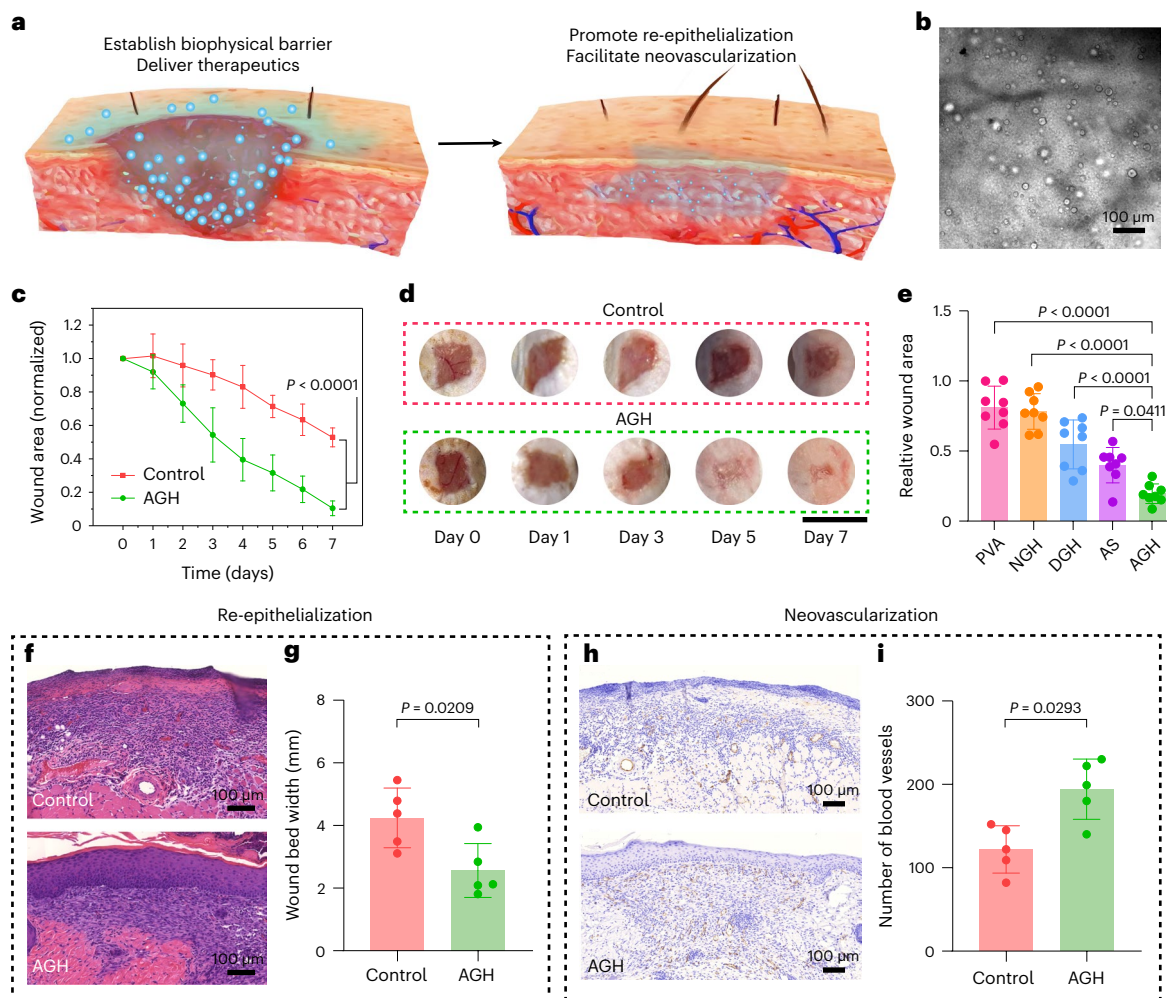


Fig. 5 | AGH accelerates the skin wound healing process in vivo. **a**, Schematic showing how granule-releasing hydrogel therapy accelerates wound healing on mouse dorsal skin. **b**, Microscopy image showing that the granular composite was fully released and attached to the wound surface after 24 h. **c**, Remaining wound areas were monitored for 7 days. On day 7, the wound area of the AGH group was significantly smaller compared with control group, indicating that the AGH accelerates the recovery process of dorsal skin wounds. $n = 8$ independent animals. **d**, Representative images of dorsal skin wounds at different time points after AGH treatment. Scale bar, 1 cm. **e**, Comparison of remaining wound areas on day 7 in the PVA, NGH, DGH, AS and AGH groups indicates that the distributed granular interface and aspirin modification promotes the therapeutic effect of the granule-releasing hydrogels. $n = 8$ independent animals. **f**, Representative H&E staining images showing re-epithelialized skin wounds on day 7 after AGH treatment. **g**, AGH treatment significantly narrowed the width of the dorsal skin wound bed on day 7 (analysis of H&E-stained sections). $n = 5$

independent animals. **h**, CD31 histochemical staining in wound tissue sections after different treatments show microvessel distribution in the wound area on day 7. **i**, Quantification analysis of blood vessels in the wound area shows that AGH promotes tissue neovascularization. $n = 5$ independent animals. PVA, mice treated with aspirin-modified starch/chitosan granules inside polyvinyl alcohol matrix; NGH, mice treated with non-granule-releasing hydrogels. The composition of NGH is the same as the AGH, but the granular structure is destroyed through gelatinization process. DGH, mice treated with unmodified dynamic granule-releasing hydrogels; AGH, mice treated with aspirin-modified granule-releasing hydrogels; AS: mice treated with aspirin-modified starch/chitosan granules without hydrogel matrix. Data are presented as mean \pm s.e.m. The P values in **c,g,i** are determined by paired t -test, two-tailed, while the P values in **e** are determined by ordinary one-way ANOVA with Tukey's multiple comparisons test.

healing involves migration, proliferation and differentiation of epithelial cells—behavior that may be regulated according to the porosity and degradation rate of substrate materials^{45,46}. In a skin wound closure model (Fig. 5a), the granule-releasing hydrogels with viscoelastic properties conformed to the irregular skin wound bed and established the initial biointerface. The aspirin-modified granule inside the matrix was slowly released over time and a granular biointerface was built up on the skin wound (Fig. 5b and Supplementary Fig. 45). The released granules had a high affinity with the skin wound bed, consistent with the ex vivo flow adhesion/affinity test (Fig. 3c).

We monitored the wound over a 7-day period and observed wound closure in AGH-treated mice (Fig. 5c,d). The PVA- and NGH-treated mice also showed the ability to promote the wound healing (Supplementary

Fig. 46). However, the therapeutic effect of the PVA and NGH group is weaker compared with the AGH group (Fig. 5e), supporting the utilities of the granular-releasing process and focal biointerfaces. DGH-treated mice also showed improved wound healing compared with the control group (Supplementary Fig. 46), but the therapeutic effect was not as strong as in the AGH-treated group (Fig. 5e). The difference in therapeutic effect may be due to the higher biological affinity of the surface-modified granules (Fig. 3c). AS alone also helped skin wound healing (Fig. 5e). However, their therapeutic effect is less compared with AGH (Supplementary Fig. 47). This is partially attributed to the initial monolithic matrix in AGH, which ensures sustained granular release and enhances the manipulation of freestanding granules, preventing material loss during treatment. Compared with the Tegaderm

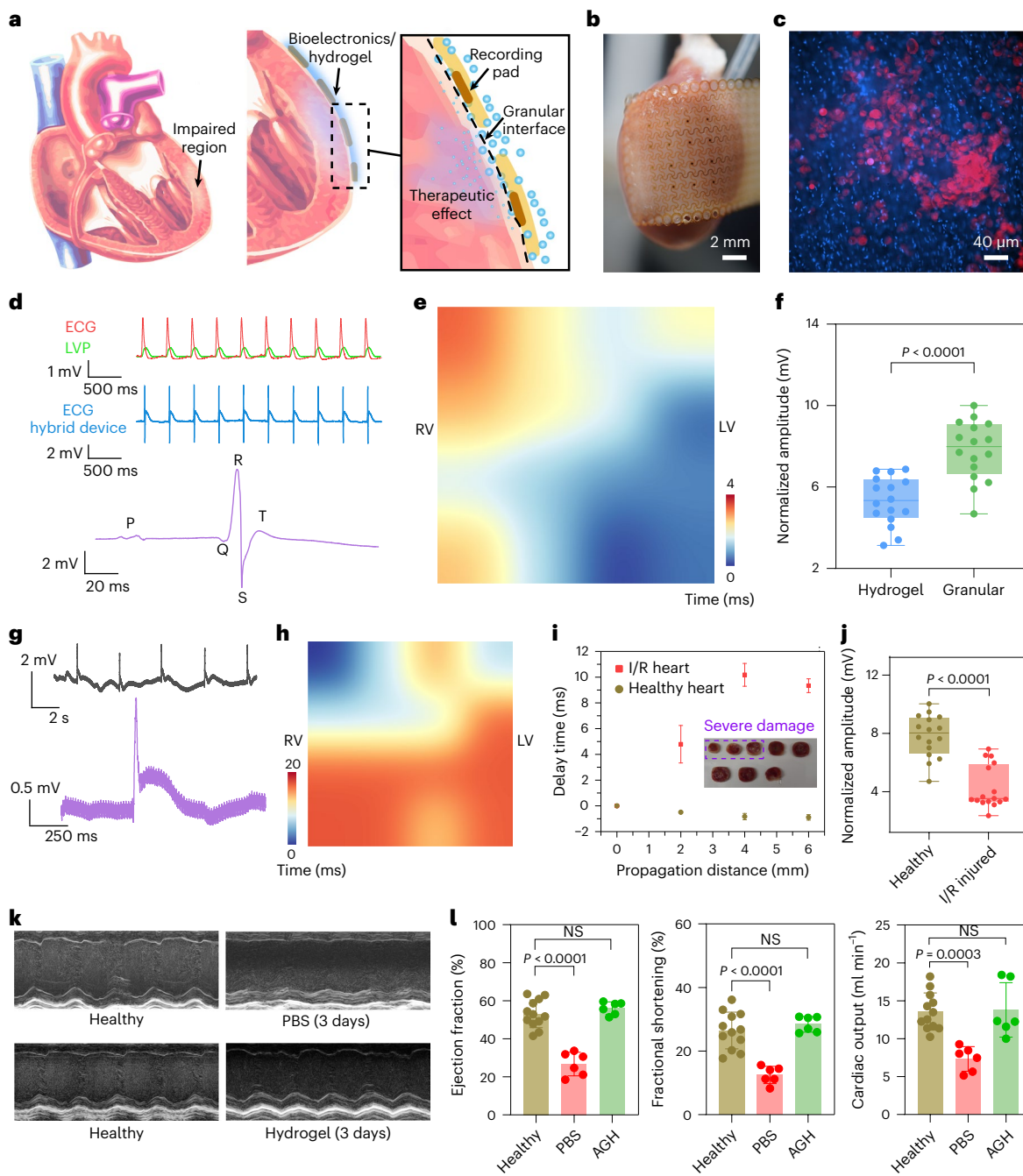


Fig. 6 | The granule-releasing hydrogel promotes mesh bioelectronics ECG recording and myocardial infarction treatment. **a**, Schematic illustrating how the granule-releasing hydrogel serves as a biointerface, adhering to heart tissue for electrophysiological recording and disease treatment. **b**, Photograph showing the configuration of a hybrid electronic device on the surface of the ex vivo heart. **c**, Fluorescence imaging shows that the granular composite (red, Alexa Fluor 647) forms a granular biointerface on the epicardium (blue, Hoechst 33342) after the phase transition of the granule-releasing hydrogel. **d**, Electrical signal of sinus rhythms from one representative electrode. Red and green, ECG signals and LVP signals recorded from iWorx, respectively; blue, ECG signals recorded from an individual channel on our multichannel electrode; purple, zoomed-in single-cycle ECG. The P, Q, R, S and T peaks are clinically defined waves that correspond to specific cardiac electrophysiological events occurring within a single heart cycle. **e**, Isochrone map ($6 \text{ mm} \times 6 \text{ mm}$ area) of the heart activation delay. LV, left ventricle; RV, right ventricle. **f**, Amplitudes of electrical signals recorded with granular interfaces are significantly higher than those collected with monolithic hydrogel interface. $n = 16$ independent channels. **g**, The electrical signal from one representative electrode shows abnormal ECG

patterns in the I/R diseased heart. Continuous (black trace) and zoom-in (purple trace) waveforms were shown. **h**, Isochrone map ($6 \text{ mm} \times 6 \text{ mm}$ area) of the I/R diseased heart. **i**, The average activation delay for longitudinal directions. $n = 4$ independent experiments. Inset: the infarct staining shows the position of heart damage, consistent with the isochrone map. **j**, Amplitudes of electrical signals recorded in the diseased I/R heart are significantly lower than those recorded in the healthy heart. $n = 16$ independent channels. **k**, Representative left-ventricle M-mode echocardiography images showing mice treated with AGH mostly recover from acute myocardial infarction. **l**, Recovery of several key indicators of cardiac function in the AGH group indicates the therapeutic effect in a myocardial infarction model. $n = 12$ independent animals for healthy group; $n = 6$ independent animals for the other groups. AGH, mice treated with aspirin-modified granule-releasing hydrogels. Data are presented as mean \pm s.e.m. The color bar indicates the heart activation delay time. All boxes bind interquartile range divided by the median; whiskers extend from minimum to maximum values. The P values in **f** and **j** are determined by paired t -test, two-tailed, while the P values in **i** are determined by ordinary one-way ANOVA with Tukey's multiple comparisons test.

dressing, the AGH appears to show a potentially enhanced therapeutic effect in wound healing (Supplementary Fig. 48).

Hematoxylin and eosin (H&E) staining revealed that AGH treatment accelerated post-injury re-epithelialization, reduced inflammatory wound bed size and promoted dermal collagen remodeling (Fig. 5f,g and Supplementary Fig. 49). In addition, the formation of new blood vessels, which supply the tissue with blood and nutrients, is crucial for proper wound healing. Neovascularization was visualized using CD31 immunohistological staining. A significantly higher number of new vessels was observed in the hydrogel-treated groups compared with the untreated group after 7 days (Fig. 5h,i and Supplementary Fig. 50). Together, these pre-clinical studies indicate that granule-releasing hydrogels may reduce inflammation and accelerate neovascularization, thereby contributing to faster wound closure and recovery.

Bioelectronic cardiac recording and tissue regeneration

The evolving hydrogels can also be integrated with bioelectronic devices to achieve both electrophysiological recording and tissue regeneration in heart tissue (Fig. 6a and Supplementary Table 1). Using gel-casting methods, we integrated a 16-channel mesh-electronic device designed for cardiac spatiotemporal mapping (Supplementary Figs. 51–53) with the AGH (Supplementary Fig. 54). The hybrid electronic device records electrical signals with an average impedance of $36.4 \Omega \text{ cm}^{-2}$ at 1 kHz over 16 channels (Supplementary Fig. 55). To demonstrate the utility of the hybrid electronic device, we interfaced it with an ex vivo heart in a Langendorff apparatus to measure the epicardial electrocardiography (Fig. 6b and Supplementary Fig. 56). Compared with surface electrocardiography, epicardial electrocardiography provides accurate localization, enabling the identification of abnormal electrical pathways, a critical aspect in guiding targeted interventions⁴⁷. Freestanding flexible mesh devices are naturally fragile and cannot be easily deployed to the living tissue surface. However, the hybrid electronic device is much more robust during macroscopic manual manipulation (Fig. 1d and Supplementary Fig. 57).

Upon temperature increase in the Langendorff apparatus, focal biointerfaces formed at the ex vivo heart tissue surface (Fig. 6c and Supplementary Fig. 58). After the activation of the isolated heart, the hybrid electronic device recorded electrograms of sinus rhythms at different positions between the right ventricle and left ventricle (Fig. 6d, and Supplementary Figs. 59 and 60) with field potential propagation pathways throughout the myocardium (Fig. 6e). The amplitudes of the cardiac signals recorded with the focal biointerfaces are statistically higher than those collected with monolithic hydrogel biointerfaces, indicating that the focal biointerface facilitates bioelectrical signal transmission to the mesh bioelectronics (Fig. 6f).

Finally, the hybrid bioelectronic device can diagnose heart disease and facilitate treatment (Fig. 6a). Ischemia/reperfusion (I/R) is a severe pathological condition that contributes to heart tissue injury and eventually leads to myocardial infarction conditions⁴⁸. Our hybrid device system can monitor electrocardiography (ECG) signals (Supplementary Fig. 61) and detect abnormal ECG signal patterns (Fig. 6g) and delayed heart electrical activation (Fig. 6h). The longer activation delay area in the isochrone map locates a severely damaged area in the I/R heart, which is consistent with the infarct staining result (Fig. 6i). Besides, the amplitudes of the cardiac signals recorded in the diseased heart are significantly lower than those collected in the healthy heart (Fig. 6j). Thus, the hybrid electronic device can diagnose abnormal heart rhythms in cases of ischemia or ventricular fibrillation (Supplementary Fig. 62). To further prove the utility of our hybrid mesh electronics in potential application in surgical epicardial electrocardiography recording, we also performed in vivo rat heart recording models. Our hybrid device system can stably adhere to the heart for ECG recording and spatiotemporal monitoring over 270 min (Supplementary Figs. 63 and 64). Besides, the recorded amplitude and the signal-to-noise ratio will not be decreased during the recording, suggesting long-term stability within the heart

surgical durations (Supplementary Fig. 65). In addition, the aspirin-modified granules adhered to the surface of the heart tissue will not damage the tissue (Supplementary Fig. 66) and promote tissue recovery from acute myocardial infarction (Fig. 6k). To demonstrate this, we applied the AGH without electronics to the infarcted hearts to investigate its therapeutic effect using a mouse acute myocardial infarction model. Echocardiography examination results from diseased mice treated with AGH showed recovery of several key indicators of cardiac function (for example, ejection fraction, fractional shortening and cardiac output) after 3 days (Fig. 6l). Furthermore, heartbeat synchronicity improved with AGH treatment (Supplementary Fig. 67). Thus, the granule-releasing hydrogel has the potential to be integrated with bioelectronic devices in disease diagnosis and treatment.

Discussion

The releasable granule-releasing hydrogels are promising as an evolving biointerface platform (Supplementary Table 1) with potential applications for inflammatory bowel disease treatment, tissue regeneration and improved flexible bioelectronics operations. Upon granular release, transient focal biointerfaces are created that might overcome the challenges associated with static monolithic materials, such as low spatiotemporal resolution, a lack of optimal biocompatibility, and/or ineffective signal transduction and molecular transport. By encapsulating granules in a responsive hydrogel matrix, we achieved improved macroscopic material/device handling in ambient conditions and responsive release of therapeutic and adhesive granules. The focal adhesion mechanism of the modified granules, inspired by the cellular or tissue affinity of drug molecules, may be extended to a wide range of monolithic or other focal adhesion interfaces for biomedical applications. Several food-grade biopolymers have been incorporated into the hydrogel composites to improve the viscoelastic behavior, and to produce direct therapeutic effects in treating ulcerative colitis, skin wounds and infarcted heart tissue. As all the materials used to construct the evolving biointerfaces are derived from natural bioresources (that is, biopolymers, and natural biomolecules such as aspirin), the granule-releasing hydrogels might offer a more cost-effective and sustainable means of addressing certain biomedical or biophysical issues. This work presents a design rule that combines the benefits and application domains of current monolithic and focal biointerface systems.

Methods

All animal procedures were approved by the Institutional Animal Care and Use Committee of the University of Chicago in protocol number 72378 (rat) and 72621 (mice).

Chemicals

The starch derived from the tapioca is purchased from Cargill. Chitosan (deacetylation degree 75–80%) and gelatin (porcine skin, type A, 300 Bloom), polyvinyl alcohol (99%+ hydrolysed, *Molecular weight (M_w)* 89,000–98,000) were purchased from Sigma-Aldrich. Tegaderm Ag Alginate Silver Dressing was purchased from 3M. Unless otherwise stated, all other chemicals were purchased from Sigma-Aldrich without further purification.

Synthesis of hydrogel composite

To prepare the dynamic granule-releasing hydrogels (DGH), the starch (16.5%), chitosan (0.83%) and acetate acid (0.83%) were added to sterilized water/phosphate-buffered saline (PBS). The suspension was stirred for 24 h at 45 °C with humidity control to hydrate the starch granules and form the starch/chitosan granules. The gelatin powder (14.18 wt%) was then added to the mixture by vigorously stirring. After 12 h, the mixture was transferred into acrylic molds with the desired shapes and sealed with acrylic cover slides for gelation at 4 °C. The dynamic granule-releasing hydrogel composite was ready after 1 h. Aspirin-modified granule-releasing hydrogels (AGH) are prepared similarly to DGH, but the chitosan is

changed to aspirin-modified chitosan. Non-granule-releasing hydrogels (NGH) are prepared by heating up the AGH over 80 °C for 2 h to destroy the starch granular shapes. The chemical composition and weight percentage of each ingredient in NGH are the same as those in the AGH. To synthesize the aspirin-modified granules with polyvinyl alcohol matrix (PVA), the aspirin-modified starch/chitosan granules was added into 10% polyvinyl alcohol solution by vigorously stirring. The mixture was poured into an acrylate mold, followed by freezing at -20 °C for 12 h and thawing at 25 °C for 2 h to form aspirin-modified granules–PVA hydrogel (PVA).

The kinetics of granular transportation

We assume that the starch granule particles trapped inside a horizontally placed hydrogel film can spontaneously transport to the bottom of the gel and contact with the biological surface. The transportation is driven by the particle's own gravity. For simplicity, we assume that the granule particles move downward at a constant velocity, U . The velocity is determined by both the gravitational force as well as the hydrodynamic drag. Although the hydrogel fluid is viscoelastic, here we ignore the elastic effect and focus on only the viscous effect. Under these circumstances, the Reynolds number, Re , of a falling particle is determined by:

$$Re = \frac{\rho_h U D_g}{\mu_h}$$

where ρ_h is the density of hydrogel, which is close to 10^3 kg m^{-3} ; D_g is the diameter of granular particles, which spans from 5 μm to 30 μm and has a main value of 14.7 μm; μ_h is the dynamic viscosity of the hydrogel as measured by rheometer at low shear rate (1 s^{-1}), which spans from 0.1 Pa s to 5,600 Pa s, depending on the hydrogel temperature and pH value. Considering that the particles are small, and the hydrogel is viscous, the flow of the particle is a laminar flow even if the dropping velocity of the sphere is as high as 1 mm s^{-1} (where Re is expected to be smaller than 10^{-4}).

For laminar flow, the drag coefficient of a sphere, C_f , versus Re is

$$C_f = \frac{24}{Re} + \frac{4}{\sqrt{Re}} + 0.4$$

Meanwhile, the drag coefficient of a sphere is:

$$C_f = \frac{8F_g}{\rho_h U^2 \pi D_g^2} = \frac{4\rho_g g D_g}{3\rho_h U^2}$$

where F_g is the drag force (which is gravitational force in this case) and ρ_g is the density of the particle which is close to $1.5 \times 10^3 \text{ kg m}^{-3}$. The final equation is therefore:

$$\frac{\rho_g g D_g}{3\rho_h} \frac{1}{U^2} = \frac{6\mu_h}{\rho_h D_g} \frac{1}{U} + \sqrt{\frac{\mu_h}{\rho_h D_g}} \frac{1}{\sqrt{U}} + 0.1$$

where $g = 9.8 \text{ m/s}^2$ represents gravitational acceleration on earth. It should be noticeable that for such a small Re ($< 10^{-4}$) value, the last two terms on the right-hand side can be ignored, because $Re^{-1} \gg Re^{-0.5}$, and $Re^{-1} \gg 0.4$. This simplifies the equation into:

$$U \approx \frac{g \rho_g D_g^2}{18\mu_h}$$

The expected falling timescale $\tau = d_h/U$, hence

$$\tau \approx \frac{18\mu_h d_h}{g \rho_g D_g^2}$$

where d_h represents the thickness of the hydrogel film. The simplified model highlights a linear relationship between the transportation time, τ ,

which is a kinetics parameter, and the hydrogel dynamic viscosity, which is affected by its temperature and pH value.

Synthesis of chitosan–drug conjugate

The chitosan–drug conjugate was synthesized with carbodiimide chemistry. The drug molecules include aspirin, nicotinic acid and butyric acid. In a typical chemical reaction with the aspirin molecule, chitosan (0.25 g) was fully dissolved into 25 ml water by adding 1 M HCl. The colloid was then vigorously stirred overnight. Then the pH of the mixture was adjusted to 4.5 by adding 1 M NaOH. Aspirin (2 mmol) was then added to the mixture while vigorously stirring. 1-Ethyl-3-(3-dimethylaminopropyl)carbodiimide (EDC) solution was prepared by dissolving 10 mmol EDC in 12 ml of a 1:1 v/v solution of ethanol and water, and the solution was added drop-wise into the chitosan and aspirin mixture solution. The reaction is conducted at room temperature for 12 h. After the evaporation of ethanol, the final product was purified by dialysis (Slide-A-Lyzer Dialysis Cassettes, 10K MWCO) against the acidified water (pH 3.5) for 48 h. Afterward, the product was dialyzed against deionized water for 3 days. After lyophilization, the product was stored at 4 °C for future use. The synthesis of the chitosan–drug conjugate was confirmed by using ^1H NMR (Bruker, 400 MHz) and FITC (Thermo NEXUS 670 Near-, Far-, and Mid-FTIR with ATR Accessory). The degree of aspirin conjugation was calculated by comparing the relative peak area of aspirin (4H, aromatic ring proton, δ 6–8, D_2O) and an acetyl group (3H, $-\text{COCH}_3$, δ 1.95, D_2O) on the backbone of chitosan.

DSS-induced colitis treatment

Eight-week-old male C57BL/6 mice were housed in groups of 5 mice per cage and acclimatized for 7 days before inclusion in the investigation. Mice were supplied with 2–3% DSS (M_w , 40 kDa; Thermo Scientific) in their drinking water for 6–10 days. The control group (healthy mice) received normal tap water. Afterward, different materials were administrated orally to the mice on predetermined days with a dose of 10 mg per kg. Before oral administration, the hydrogel is sliced into small pieces using a scalpel and then loaded into a 16-gauge gavage needle. For the experiments of the PVA, DGH, AS and AGH groups, an equal amount of the granules was applied. 5-Aminosalicylic acid was suspended in a viscous carboxymethyl cellulose solution with a concentration of 10 mg ml^{-1} . During the experiment, changes in body weight were recorded daily, and feces were collected daily to assess bleeding. The mice were euthanized on the last day of the experiment and their entire colon was collected. After a gentle wash with physiological saline, the colon length was measured. The histological evaluation of the colon was also performed. On the last day, feces were also collected for water content analysis and microbiome analysis. In vivo experiments related to butyric acid and nicotinic acid conjugations are performed in a similar approach.

Histology

For tissue histological analysis, PAS, H&E and CD31 histological tissue sections were prepared by the Human Tissue Resource Center at the University of Chicago. Tissue sections of the proximal and distal colon were prepared and stained with PAS and H&E. Tissue sections of the epidermal skin were prepared and stained with CD31 and H&E. All the tissue histological results are analyzed by the CaseViewer software (3DHISTECH). The colonic histological damage was scored based on the H&E-stained colonic tissue sections: severity of inflammation (0, none; 1, slight; 2, moderate; 3, severe), the extent of injury (0, none; 1, mucosal; 2, mucosal and submucosal; 3, transmural) and crypt damage (0, none; 1, basal one-third damaged; 2, basal two-thirds damaged; 3, only surface epithelium intact; 4, entire crypt and epithelium lost). Scores from all three perspectives were summed, resulting in a total histological scoring range of 0 to 10.

Skin wound model

C57BL/6 mice (8–10 weeks) mice were anesthetized with isoflurane and then two partial-thickness wounds with 5 mm × 5 mm were made

on the dorsal skin of the mice. Full-thickness wounds on the dorsum of the mice were created by using 6 mm biopsy punches. After that, one side of wound was applied with hydrogel and the other side was treated with PBS buffer. Then wounds are covered by band-aid bandage. The hydrogel is applied every day for seven consecutive days and the remaining wound area from both sides are recorded. On day 7, the mice were euthanized and the wound skin tissue was collected for histological analysis. For the experiments of the PVA, DGH, AS and AGH groups, an equal amount of the granules was applied. Wound area ($\text{Area}_{\text{Day}x}$) was determined using ImageJ software by a blinded observer. Wound area (normalized) for each wound is calculated by:

$$\text{Wound area (Normalized)} = \frac{\text{Area}_{\text{Day}x}}{\text{Area}_{\text{Day}0}} \times 100\%$$

Relative wound area is used to compare the therapeutic effects of treatment between the groups:

$$\text{Relative wound area} = \frac{\text{Area}_{\text{experiment}}}{\text{Area}_{\text{control}}} \times 100\%$$

Mesh-electronic and hydrogel hybrid fabrication

The 3-layer 16-channel recording electrodes were fabricated on the p-type wet oxide silicon wafer (HS39626-WO, NOVA Electronic Materials) served as the substrate and the wet oxide as the sacrificial layer. Photomasks were designed in AutoCAD 2021. A schematic of the micro-fabrication procedure is illustrated in Supplementary Figs. 51–53. The first SU-8 layer (SU-8 3025, MicroChem), which has a thickness of approximately 22 μm , was patterned with serpentine-like geometries using direct writer photolithography (MLA150, Heidelberg). The first layer serves as flexible and stretchable support for the electrode. On top of the first layer, the metal layers with 5 nm Cr and 100 nm A, were evaporated using an electron-beam evaporator (EvoVac, Angstrom Engineering) on the patterned AZ nlof 2070 (MicroChem) photoresist mask followed by a lift-off in AZ NMP (MicroChem) to remove the photoresist. Next, the third encapsulation layer (SU-8 3005, MicroChem), which has a thickness of approximately 8 μm , was patterned to encapsulate the metal interconnects and exposed only the sensing pads to interface cardiac tissues and bottom pads for zero-insertion-force connection. Finally, the device was lifted off in a buffered HF bath, which removed the sacrificial wet oxide layer. To make the hydrogel hybrid devices, the mesh-electronic was first attached to the PDMS. Then hydrogel precursor solution was spin-coated to the PDMS surface at 1,000 rpm at 40 °C. After cooling and trimming, the hydrogel hybrid devices were peeled off from the substrate.

Ex vivo heart signal recording experiment

An adult rat was heparinized by intraperitoneal injection with a concentration of 1,000 IU per kg and rested for 20 min. An open-drop exposure of isoflurane was used in a bell jar to anesthetize the rat. Hearts were collected and placed in cold HBSS buffer, with the aorta cannulated in preparation for use in the Langendorff set-up. The cannulated aorta was perfused with oxygenated HEPES-buffered Tyrode's solution (recipe: KCl, 5.4 mM; NaCl, 126 mM; glucose, 10 mM; MgCl₂, 1 mM; HEPES, 10 mM; MgSO₄, 1.2 mM; CaCl₂, 2 mM; NaH₂PO₄, 0.39 mM; bubbled with 99.5% O₂; pH 7.3). The heart was mounted in a water-jacketed beaker (Fisher Scientific) to maintain at 37 °C and the perfusion was passed through a heating coil and bubble trap (Radnoti). By adjusting the height of the intravenous bag containing the perfusion buffer, the perfusion pressure was kept between 80 mm Hg and 100 mm Hg. The sinoatrial node along with the atria was removed, resulting in the slowing down of the atrioventricular pace. BP-100 probes (iWorx) were connected to the perfusion line and water-filled balloons (Radnoti) were inserted into the left ventricle to monitor perfusion and

pressure in the left ventricle, respectively. Reference ECG recordings (from iWorx) were conducted by placing needle electrodes on the left ventricular wall and aorta, grounding them, and connecting them to a C-ISO-256 preamplifier (iWorx). We amplified all signals (perfusion, left ventricular pressure (LVP) and ECG) with an IA-400D amplifier (iWorx) and interfaced them with a computer using a Digidata 1550 digitizer and Clampex software (Molecular Devices). The mesh-electronic–hydrogel hybrid was placed between the left and right ventricular wall with seamless integration through the adhesion of the hydrogel. A 4 × 4 microelectrode array (2 mm spacing between electrodes) was used for the electrical mapping process and the recording was performed via a USB interface board controlled by Intan RHX software and RHD2132 16-channel input recording headstage (Intantech). Electrophysiology data for the hydrogel interface are recorded immediately after positioning the hybrid device on the heart. For the granular interface, data are gathered once the interface is fully established. This typically occurs around 10 min considering the thickness of the coated hydrogel (350–550 μm). For the ex vivo isolated heart experiment, the continuous perfusion water flush over the heart at the Langendorff set-up can slightly accelerate the granule release process. The ECG amplitudes were baseline calibrated and averaged from more than 20 ECG peaks for each of the 16 individual channels. The normalized amplitudes/noise values were calculated by dividing the largest depolarization peak by the standard deviation of the baseline (noise). The isochrone maps of the electrical propagation were plotted from averaging more than 20 ECG peaks from all 16 channels. All calculations were performed using Python scripts. To improve readability, we used Gaussian interpolation for map rendering.

Murine acute myocardial infarction model

All the surgical procedures to induce mice acute myocardial infarction were performed in the University of Illinois at Chicago Cardiovascular Research Core. Before surgery, mice were weighed and subcutaneously injected with buprenorphine SR LAB (1.0 mg per kg). Following isoflurane anesthesia, the heart was exposed by performing a left thoracotomy through the fourth intercostal space. The left anterior descending coronary artery was identified and temporally ligated. After 45 min, the ligature was released and the reperfusion phase began. Then 40 mm³ aspirin-modified granule-releasing hydrogel was applied to peri-infarct area within 5 min after reperfusion into each mouse. PBS was used as a negative control. The thoracotomy site was closed, and positive end expiratory pressure was increased to hyperinflate the lungs. The animals were observed and studied for 3 days post-surgery.

Statistical analysis

ImageJ 1.52a was used to process and analyze all the image data and GraphPad Prism software (v. 8 and v. 9.4.1) was used for all statistical analysis. Plotting was performed with Origin 2019b, MATLAB R2021b and Adobe Illustrator 2022. Laser confocal scanning microscopy images were analyzed with OLYMPUS OLS 5000 1.1.1.55. All the error bar indicates the standard deviation unless otherwise stated. Multiple *t*-tests or one-way analysis of variance (ANOVA) were performed for all the biological data analysis. A value of *P* < 0.05 was considered statistically significant.

Reporting summary

Further information on research design is available in the Nature Portfolio Reporting Summary linked to this article.

Data availability

All data supporting the findings of this study are available within the article and its Supplementary Information. Data are also available from the corresponding authors upon reasonable request. Source data are provided with this paper. All Source Data are also available at https://osf.io/tns4k/?view_only=2bac0651e0f84f62acd95d490c773c31.

Code availability

Custom code used in this study is available at <https://github.com/sjiuyun/Code-Availability>.

References

1. Elnathan, R. et al. Biointerface design for vertical nanoprobes. *Nat. Rev. Mater.* **5**, 41578-022-00464-7 (2022).
2. Zhang, S. F. et al. An inflammation-targeting hydrogel for local drug delivery in inflammatory bowel disease. *Sci. Transl. Med.* <https://doi.org/10.1126/scitranslmed.aaa5657> (2015).
3. Nan, K. et al. Mucosa-interfacing electronics. *Nat. Rev. Mater.* <https://doi.org/10.1038/s41578-022-00477-2> (2022).
4. Jiang, Y. W. et al. Topological supramolecular network enabled high-conductivity, stretchable organic bioelectronics. *Science* **375**, 1411–1417 (2022).
5. Wang, X. et al. A nanofibrous encapsulation device for safe delivery of insulin-producing cells to treat type 1 diabetes. *Sci. Transl. Med.* <https://doi.org/10.1126/scitranslmed.abb4601> (2021).
6. Armstrong, J. P. K. et al. A blueprint for translational regenerative medicine. *Sci. Transl. Med.* <https://doi.org/10.1126/scitranslmed.aaz2253> (2020).
7. Yang, Q. S. et al. Photocurable bioresorbable adhesives as functional interfaces between flexible bioelectronic devices and soft biological tissues. *Nat. Mater.* **20**, 1559–1570 (2021).
8. Kim, D. H. et al. Epidermal electronics. *Science* **333**, 838–843 (2011).
9. Yang, Y. Y. et al. Wireless multilateral devices for optogenetic studies of individual and social behaviors. *Nat. Neurosci.* **24**, 1035–1045 (2021).
10. Freedman, B. R. et al. Enhanced tendon healing by a tough hydrogel with an adhesive side and high drug-loading capacity. *Nat. Biomed. Eng.* <https://doi.org/10.1038/s41551-021-00810-0> (2022).
11. Deng, J. et al. Electrical bioadhesive interface for bioelectronics. *Nat. Mater.* **20**, 229–236 (2021).
12. Tringides, C. M. et al. Viscoelastic surface electrode arrays to interface with viscoelastic tissues. *Nat. Nanotechnol.* **16**, 1019–1029 (2021).
13. Lin, X. et al. A viscoelastic adhesive epicardial patch for treating myocardial infarction. *Nat. Biomed. Eng.* **3**, 632–643 (2019).
14. Brannon, E. R. et al. Polymeric particle-based therapies for acute inflammatory diseases. *Nat. Rev. Mater.* **7**, 796–813 (2022).
15. Lueckgen, A. et al. Enzymatically-degradable alginate hydrogels promote cell spreading and in vivo tissue infiltration. *Biomaterials* <https://doi.org/10.1016/j.biomaterials.2019.119294> (2019).
16. Griffin, D. R., Weaver, W. M., Scumpia, P. O., Di Carlo, D. & Segura, T. Accelerated wound healing by injectable microporous gel scaffolds assembled from annealed building blocks. *Nat. Mater.* **14**, 737–744 (2015).
17. Chen, J. et al. Pollen-inspired enzymatic microparticles to reduce organophosphate toxicity in managed pollinators. *Nat. Food* **2**, 339–347 (2021).
18. Tang, J. A. et al. Therapeutic microparticles functionalized with biomimetic cardiac stem cell membranes and secretome. *Nat. Commun.* **8**, 13724 (2017).
19. Gattazzo, F., Urciuolo, A. & Bonaldo, P. Extracellular matrix: a dynamic microenvironment for stem cell niche. *Biochim. Biophys. Acta* **1840**, 2506–2519 (2014).
20. Koo, J. et al. Wireless bioresorbable electronic system enables sustained nonpharmacological neuroregenerative therapy. *Nat. Med.* **24**, 1830–1836 (2018).
21. Allen, M. E., Hindley, J. W., Baxani, D. K., Ces, O. & Elan, Y. Hydrogels as functional components in artificial cell systems. *Nat. Rev. Chem.* **6**, 562–578 (2022).
22. Daly, A. C., Riley, L., Segura, T. & Burdick, J. A. Hydrogel microparticles for biomedical applications. *Nat. Rev. Mater.* **5**, 20–43 (2020).
23. Xu, Y. X., Kim, K. M., Hanna, M. A. & Nag, D. Chitosan-starch composite film: preparation and characterization. *Ind. Crop Prod.* **21**, 185–192 (2005).
24. Masina, N. et al. A review of the chemical modification techniques of starch. *Carbohydr. Polym.* **157**, 1226–1236 (2017).
25. Li, J. X. et al. A tissue-like neurotransmitter sensor for the brain and gut. *Nature* **606**, 94–101 (2022).
26. Guimaraes, C. F., Gasperini, L., Marques, A. P. & Reis, R. L. The stiffness of living tissues and its implications for tissue engineering. *Nat. Rev. Mater.* **5**, 351–370 (2020).
27. Fang, Y. et al. Dynamic and programmable cellular-scale granules enable tissue-like materials. *Mater.* **2**, 948–964 (2020).
28. Park, B. et al. Cuticular pad-inspired selective frequency damper for nearly dynamic noise-free bioelectronics. *Science* **376**, 624–629 (2022).
29. Du, H. L., Liu, M. R., Yang, X. Y. & Zhai, G. X. The design of pH-sensitive chitosan-based formulations for gastrointestinal delivery. *Drug Discov. Today* **20**, 1004–1011 (2015).
30. Dabrowska, M., Starek, M. & Skucinski, J. Lipophilicity study of some non-steroidal anti-inflammatory agents and cephalosporin antibiotics: a review. *Talanta* **86**, 35–51 (2011).
31. Galie, P. A. et al. Fluid shear stress threshold regulates angiogenic sprouting. *Proc. Natl Acad. Sci. USA* **111**, 7968–7973 (2014).
32. Kobayashi, T. et al. Ulcerative colitis. *Nat. Rev. Dis. Primers* **6**, 74 (2020).
33. Jeong, D. Y. et al. Induction and maintenance treatment of inflammatory bowel disease: a comprehensive review. *Autoimmun. Rev.* **18**, 439–454 (2019).
34. Chassaing, B., Aitken, J. D., Malleshappa, M. & Vijay-Kumar, M. Dextran sulfate sodium (DSS)-induced colitis in mice. *Curr. Protoc. Immunol.* **104**, 15.25.11–15.25.14 (2014).
35. Diao, Y. J. et al. Effect of interactions between starch and chitosan on waxy maize starch physicochemical and digestion properties. *CyTA J. Food* **15**, 327–335 (2017).
36. Cao, Y. P. & Mezzenga, R. Design principles of food gels. *Nat. Food* **1**, 106–118 (2020).
37. Ni, J., Wu, G. D., Albenberg, L. & Tomov, V. T. Gut microbiota and IBD: causation or correlation? *Nat. Rev. Gastroenterol. Hepatol.* **14**, 573–584 (2017).
38. Round, J. L. & Mazmanian, S. K. The gut microbiota shapes intestinal immune responses during health and disease. *Nat. Rev. Immunol.* **9**, 313–323 (2009).
39. Fabia, R. et al. Impairment of bacterial-flora in human ulcerative-colitis and experimental colitis in the rat. *Digestion* **54**, 248–255 (1993).
40. Zhang, Z. et al. Chlorogenic acid ameliorates experimental colitis by promoting growth of akkermansia in mice. *Nutrients* <https://doi.org/10.3390/nu9070677> (2017).
41. Osman, N., Adawi, D., Ahrne, S., Jeppsson, B. & Molin, G. Modulation of the effect of dextran sulfate sodium-induced acute colitis by the administration of different probiotic strains of *Lactobacillus* and *Bifidobacterium*. *Digest. Dis. Sci.* **49**, 320–327 (2004).
42. Geier, M. S., Butler, R. N., Giffard, P. M. & Howarth, G. S. *Lactobacillus fermentum* BR11, a potential new probiotic, alleviates symptoms of colitis induced by dextran sulfate sodium (DSS) in rats. *Int. J. Food Microbiol.* **114**, 267–274 (2007).
43. Sostres, C. & Lanas, A. Gastrointestinal effects of aspirin. *Nat. Rev. Gastroenterol. Hepatol.* **8**, 385–394 (2011).
44. Zhang, W. et al. Catechol-functionalized hydrogels: biomimetic design, adhesion mechanism, and biomedical applications. *Chem. Soc. Rev.* **49**, 433–464 (2020).

45. Griffin, D. R. et al. Activating an adaptive immune response from a hydrogel scaffold imparts regenerative wound healing. *Nat. Mater.* **20**, 560–569 (2021).
46. Gurtner, G. C., Werner, S., Barrandon, Y. & Longaker, M. T. Wound repair and regeneration. *Nature* **453**, 314–321 (2008).
47. Park, J. et al. Electromechanical cardioplasty using a wrapped elasto-conductive epicardial mesh. *Sci. Transl. Med.* <https://doi.org/10.1126/scitranslmed.aad8568> (2016).
48. Thygesen, K. et al. Third universal definition of myocardial infarction. *Nat. Rev. Cardiol.* **9**, 620–633 (2012).

Acknowledgements

We thank K. Watters for scientific editing of the paper. B.T. acknowledges support from the US Air Force Office of Scientific Research (FA9550-20-1-0387), the National Science Foundation (NSF MPS-2121044) and the US Army Research Office (W911NF-21-1-0090). B.T. and J.Y. acknowledge support from the GI research foundation. P.K. acknowledges support from the National Science Foundation (DMR 2212123). Use of the Advanced Photon Source and the Center for Nanoscale Materials, both US Department of Energy Office of Science User Facilities, was supported by the US Department of Energy, Office of Science, under contract no. DE-AC02-06CH11357. H.-M.T. acknowledges the support from the Integrated Small Animal Imaging Research Resource (iSAIRR) at the University of Chicago. Parts of this work were carried out at the Soft Matter Characterization Facility of the University of Chicago. Parts of the diagrams in Fig. 1f and Fig. 4b were created with [BioRender.com](#). We thank A. Tokmakoff and X.-x. Zhang for their support and helpful discussions.

Author contributions

B.T., J.Y., P.K. and E.B.C. supervised the research. J.S., J.Y. and B.T. conceived the idea. J.S., Y. Lin, J.Y. and B.T. developed the methods. J.S., Y. Lin, P.L., C.S., K.P., S.K., B.A., L.M., Y. Luo, S.C., H.-M.T., C.M.C., J.Z., Z.C., J.A.A.-H., J.C. and J.Y. performed the experiments. P.M.

and P.K. performed the simulation. J.M., Y. Luo, S.C., H.-M.T. and P.G. analyzed and processed the data. J.S., Y. Lin, J.Y. and B.T. wrote the paper with comments from all authors.

Competing interests

The authors declare no competing interests.

Additional information

Supplementary information The online version contains supplementary material available at <https://doi.org/10.1038/s44286-023-00008-y>.

Correspondence and requests for materials should be addressed to Petr Král, Jiping Yue or Bozhi Tian.

Peer review information *Nature Chemical Engineering* thanks Eric Appel, Youn Soo Kim and the other, anonymous, reviewer(s) for their contribution to the peer review of this work.

Reprints and permissions information is available at www.nature.com/reprints.

Publisher's note Springer Nature remains neutral with regard to jurisdictional claims in published maps and institutional affiliations.

Springer Nature or its licensor (e.g. a society or other partner) holds exclusive rights to this article under a publishing agreement with the author(s) or other rightsholder(s); author self-archiving of the accepted manuscript version of this article is solely governed by the terms of such publishing agreement and applicable law.

© The Author(s), under exclusive licence to Springer Nature America, Inc. 2024

Reporting Summary

Nature Portfolio wishes to improve the reproducibility of the work that we publish. This form provides structure for consistency and transparency in reporting. For further information on Nature Portfolio policies, see our [Editorial Policies](#) and the [Editorial Policy Checklist](#).

Statistics

For all statistical analyses, confirm that the following items are present in the figure legend, table legend, main text, or Methods section.

n/a Confirmed

- The exact sample size (n) for each experimental group/condition, given as a discrete number and unit of measurement
- A statement on whether measurements were taken from distinct samples or whether the same sample was measured repeatedly
- The statistical test(s) used AND whether they are one- or two-sided
Only common tests should be described solely by name; describe more complex techniques in the Methods section.
- A description of all covariates tested
- A description of any assumptions or corrections, such as tests of normality and adjustment for multiple comparisons
- A full description of the statistical parameters including central tendency (e.g. means) or other basic estimates (e.g. regression coefficient) AND variation (e.g. standard deviation) or associated estimates of uncertainty (e.g. confidence intervals)
- For null hypothesis testing, the test statistic (e.g. F , t , r) with confidence intervals, effect sizes, degrees of freedom and P value noted
Give P values as exact values whenever suitable.
- For Bayesian analysis, information on the choice of priors and Markov chain Monte Carlo settings
- For hierarchical and complex designs, identification of the appropriate level for tests and full reporting of outcomes
- Estimates of effect sizes (e.g. Cohen's d , Pearson's r), indicating how they were calculated

Our web collection on [statistics for biologists](#) contains articles on many of the points above.

Software and code

Policy information about [availability of computer code](#)

Data collection The fluorescence imaging data were collected with MAPS (v. 1.8), an IDL-based program developed in-house (J. Phys. IV Proc. 2003, 104, 635–638). Intan RHX software (v.3.0.4) was used for collecting electro-physiological data. DigiData 1550 digitizer was controlled using Clampex software (v. 10.4.0.36, Molecular Devices). Intantech RHD USB interface board was controlled using Intan RHX software (v. 3.0.4, Intantech).

Data analysis Plotting were performed with Origin 2019b (32-bit) 9.6.5.169 and Adobe Illustrator 21.0.0. Optical microscopy data was analyzed using ImageJ 1.52a. Tomography reconstruction was done using the gridrec algorithm in an open-source software named TomoPy. Laser confocal scanning microscope images were analyzed with OLYMPUS OLS 5000 1.1.1.55. Micro-CT data were analyzed using VivoQuant 4 patch 1 (InviCRO, LLC, Boston, USA). Histology images and data were analyzed with CaseViewer 2.4. The fittings were done using Trust-region algorithm in the commercial software MATLAB R2021b. The MD simulation was done by using NAMD 2.13 and the CHARMM36 protein force field. Photomasks were designed in AutoCAD 2021 (v. R.47.0.0). DADA2 (v. 1.26.0) was used to infer unique amplicon sequence variants from raw reads. Uclust from Qiime (v. 1.9.1) was used for taxonomy assignment. Analysis of electro-physiology data was performed with Python (v. 3.8.5) scripts using Numpy (v. 1.22.1), pandas (v. 1.1.3), matplotlib (v. 3.3.2), scipy (v. 1.9.3). The code is available at <https://github.com/sjiuyun/Code-Availability>. Echocardiography data was analyzed by the Vevo 2100 Imaging System. Statistical analysis was performed with Graphpad Prism software (v. 8 & v. 9.4.1).

For manuscripts utilizing custom algorithms or software that are central to the research but not yet described in published literature, software must be made available to editors and reviewers. We strongly encourage code deposition in a community repository (e.g. GitHub). See the Nature Portfolio [guidelines for submitting code & software](#) for further information.

Data

Policy information about [availability of data](#)

All manuscripts must include a [data availability statement](#). This statement should provide the following information, where applicable:

- Accession codes, unique identifiers, or web links for publicly available datasets
- A description of any restrictions on data availability
- For clinical datasets or third party data, please ensure that the statement adheres to our [policy](#)

All data supporting the findings of this study are available within the Article, its Supplementary Information. Data are also available from the corresponding authors upon reasonable request. Statistical source data are provided with this Paper. All source data are also available at https://osf.io/tns4k/?view_only=2bac0651e0f84f62acd95d490c773c31.

Human research participants

Policy information about [studies involving human research participants and Sex and Gender in Research](#).

Reporting on sex and gender

N/A

Population characteristics

N/A

Recruitment

N/A

Ethics oversight

N/A

Note that full information on the approval of the study protocol must also be provided in the manuscript.

Field-specific reporting

Please select the one below that is the best fit for your research. If you are not sure, read the appropriate sections before making your selection.

Life sciences

Behavioural & social sciences

Ecological, evolutionary & environmental sciences

For a reference copy of the document with all sections, see nature.com/documents/nr-reporting-summary-flat.pdf

Life sciences study design

All studies must disclose on these points even when the disclosure is negative.

Sample size

Animal numbers for each experiment are provided in the figure captions. Each quantitative experiment was performed in at least 5 replicates. No sample-size calculation was performed for the in vivo studies. The expected effect sizes were large, and therefore 5 replicates were fully sufficient.

Data exclusions

Representative images were shown in the manuscripts; similar results from experimental repeats were not shown. No data excluded from statistical analyses.

Replication

All experimental were replicated for at least three times and performed independently.

Randomization

All animals and biosamples were randomly allocated into different experimental groups.

Blinding

Experimenters were blinded during life sciences study design. All subsequent sample processing was done blinded.

Reporting for specific materials, systems and methods

We require information from authors about some types of materials, experimental systems and methods used in many studies. Here, indicate whether each material, system or method listed is relevant to your study. If you are not sure if a list item applies to your research, read the appropriate section before selecting a response.

Materials & experimental systems

n/a	Involved in the study
<input checked="" type="checkbox"/>	Antibodies
<input type="checkbox"/>	Eukaryotic cell lines
<input checked="" type="checkbox"/>	Palaeontology and archaeology
<input type="checkbox"/>	Animals and other organisms
<input checked="" type="checkbox"/>	Clinical data
<input checked="" type="checkbox"/>	Dual use research of concern

Methods

n/a	Involved in the study
<input checked="" type="checkbox"/>	ChIP-seq
<input checked="" type="checkbox"/>	Flow cytometry
<input checked="" type="checkbox"/>	MRI-based neuroimaging

Eukaryotic cell lines

Policy information about [cell lines](#) and [Sex and Gender in Research](#)

Cell line source(s)

Hacat cells were purchased from Thermo and Caco-2 cells were purchased from ATCC. Mouse colon organoid was cultured from the cells extracted from 6-8 week old C57BL/6J male mice. Human ileum organoid was cultured from the cells extracted from a female adult.

Authentication

Commercially purchased cell lines were not authenticated by study participants. Primary organoids were authenticated by the study participants.

Mycoplasma contamination

All cell lines were tested negative for mycoplasma contamination.

Commonly misidentified lines (See [ICLAC](#) register)

No commonly misidentified cell lines were used in the study.

Animals and other research organisms

Policy information about [studies involving animals](#); [ARRIVE guidelines](#) recommended for reporting animal research, and [Sex and Gender in Research](#)

Laboratory animals

6-8 week old C57BL/6J mice (female and male) purchased from the Jackson Laboratory were used in animal experiments. Mice were housed in the animal facility of the University of Chicago. The animal room was maintained in an environment with the humidity of 40-60 % and the temperature of 18-23 °C under a 12-h light/12-h dark cycle. The animals were allowed free access to food and water. Adult (10-16 weeks) Sprague-Dawley rats (female and male) originally obtained from Charles River were housed and bred in the animal facility at the University of Chicago. The animal room was maintained in an environment with the humidity of 40-60 % and the temperature of 18-23 °C under a 12-h light/12-h dark cycle. The rat were used as the heart donors for ex-vivo and in-vivo heart experiments.

Wild animals

No wild animals were used in the study.

Reporting on sex

All animal experiments were done using mice of both genders. The percentages of males and females throughout all experimental groups were the same. Therefore, sex was not considered as a variable.

Field-collected samples

No field collected samples were used in the study.

Ethics oversight

All animals were housed under pathogen-free conditions and all animal procedures were approved by the Institutional Animal Care and Use Committees (IACUC) of the University of Chicago.

Note that full information on the approval of the study protocol must also be provided in the manuscript.